The Astrophysical Journal, 792:72 (15pp), 2014 September 1 doi:10.1088/0004-637X/792/1/72

SPATIALLY RESOLVED SPECTRA OF THE "TEACUP" ACTIVE GALACTIC NUCLEUS: TRACING THE HISTORY OF A DYING QUASAR

J. P. Gagne[1], D. M. Crenshaw[1], S. B. Kraemer[2], H. R. Schmitt[3], W. C. Keel[4], S. Rafter[5], T. C. Fischer[1], V. N. Bennert[6], and K. Schawinski[7]

[1] Department of Physics and Astronomy, Georgia State University, Astronomy Offices, 25 Park Place South SE, Suite 600, Atlanta, GA 30303, USA; gagne@chara.gsu.edu

[2] Department of Physics, Catholic University of America, 620 Michigan Avenue, N.E., Washington, DC 20064, USA

[3] Naval Research Laboratory, Washington, DC 20375, USA

[4] Department of Physics and Astronomy, University of Alabama, Box 870324, Tuscaloosa, AL 35487, USA

[5] Physics Department, Technion, Haifa 32000, Israel

[6] Physics Department, California Polytechnic State University San Luis Obispo, CA 93407, USA

[7] Institute for Astronomy, Department of Physics, ETH Zurich, Wolfgang-Pauli-Strasse 27, CH-8093 Zurich, Switzerland

Received 2013 December 16; accepted 2014 July 2; published 2014 August 18

ABSTRACT

The Sloan Digital Sky Survey (SDSS) Galaxy Zoo project has revealed a number of spectacular galaxies possessing extended emission-line regions (EELRs), the most famous being Hanny's Voorwerp galaxy. We present another EELR object discovered in the SDSS endeavor: the Teacup active galactic nucleus (AGN). Nicknamed for its EELR, which has a "handle"-like structure protruding 15 kpc into the northeast quadrant of the galaxy. We analyze the physical conditions of this galaxy with long-slit, ground-based spectroscopy from the Lowell, Lick, and KPNO observatories. With the Lowell 1.8 m Perkin's telescope we took multiple observations at different offset positions, allowing us to recover spatially resolved spectra across the galaxy. Line diagnostics indicate the ionized gas is photoionized primarily by the AGN. Additionally we are able to derive the hydrogen density from the [S II] λ6716/λ6731 ratio. We generated two-component photoionization models for each spatially resolved Lowell spectrum. These models allow us to calculate the AGN bolometric luminosity seen by the gas at different radii from the nuclear center of the Teacup. Our results show a drop in bolometric luminosity by more than two orders of magnitude from the EELR to the nucleus, suggesting that the AGN has decreased in luminosity by this amount in a continuous fashion over 46,000 yr, supporting the case for a dying AGN in this galaxy independent of any IR based evidence. We demonstrate that spatially resolved photoionization modeling could be applied to EELRs to investigate long timescale variability.

Key words: cosmic rays – galaxies: active – galaxies: kinematics and dynamics – galaxies: Seyfert – quasars: emission lines – techniques: spectroscopic

Online-only material: color figures

1. INTRODUCTION

The Teacup active galactic nucleus (AGN; SDSS J143029.88+133912.0, 2MASX J14302986+1339117) was originally discovered by Massimo Mezzoprete[8] in 2007 as part of the Sloan Digital Sky Survey (SDSS) Galaxy Zoo project (Keel et al. 2012a). One of the campaigns during the Galaxy Zoo project was to find AGNs hosting extended emission-line regions (EELRs), gaseous regions that are AGN-ionized at distances of ∼10 kpc. Spectroscopically confirmed as an EELR by Keel et al. (2012a), the Teacup possesses a redshift of $z = 0.086$ to yield a distance of 344 Mpc ($1'' \sim 1.7$ kpc for $H_0 = 73\,\mathrm{km\,s^{-1}\ Mpc^{-1}}$). The "Teacup" nickname was given to describe its EELR, a spectacular "handle" or loop of ionized gas extending out to ∼15 kpc northeast from the nucleus of the galaxy, a feature best seen via *Hubble Space Telescope* (*HST*) imaging (Keel et al. 2013; also posted online[9]). EELRs offer a unique way to study AGNs, by allowing us to study ionization interactions between the central AGN engine and exterior regions of the galaxy.

We use multiple sources of data available to us, the first being images and spectra from the SDSS. In Figure 1, we show the SDSS image from the *g*, *r*, and *i* bandpasses combined; in the northeast corner the ionized handle is visible as a purple loop, which can also be seen in the contour map. The continuum emission shows a somewhat disturbed morphology, possibly from a merger or some other interaction. Figure 2 shows a spectrum of the optical center of the galaxy taken from SDSS with a spectral resolving power of $R \equiv \lambda/\Delta\lambda \approx 2000$ and a 3″ diameter fiber; strong emission lines characteristic of AGN-ionized gas are present. Figure 3 presents one of our spectra taken from Lowell Observatory at 5″ east from center, intersecting the loop structured EELR. To explain the color of this feature in the SDSS image, *g*, *r*, and *i* filter response curves are overplotted. Note that the *g* filter has been color coded as blue, *r* as green, and *i* as red. Interestingly, [O III] λ5007 falls in between the *g* and *r* bandpass filters. Because the rest of the emission lines fall inside the ranges of both the *g* and *i* filters while redshifted, λ5007, the strongest emission line, is clipped out by the bandpasses, the ionized handle of gas in the NE shown in purple in Figure 1, as does the ionized gas in the SW and other portions of the galaxy. The spectrum is typical of a type 2 AGN (Khachikian & Weedman 1971), with strong emission lines covering a broad range in ionization, a weak continuum with several stellar absorption features, and no evidence for broad (FWHM $\geqslant 1000$ km s^{-1}) emission lines.

In this paper, we present results from long-slit spectroscopic and imaging observations from the Lowell, KPNO, Lick, SDSS and VLA observatories. The data provide an exciting

[8] http://www.galaxyzooforum.org/index.php?%20topic=7539.msg62340

[9] http://blog.galaxyzoo.org/2012/06/14/hubble-spies-the-teacup-and-i-spy-hubble/

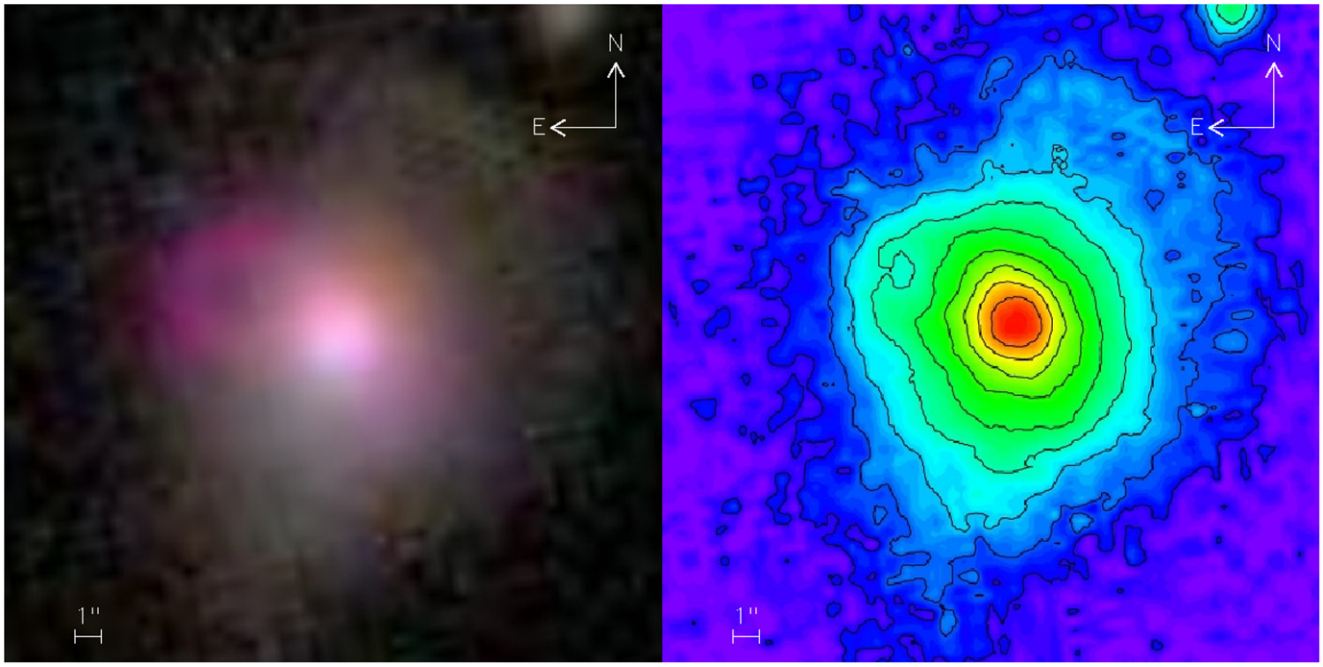

Figure 1. Original Sloan optical image on the left, showing an ionized handle of gas in the northeast region of the galaxy in purple. Right: the same SDSS image with contours overplotted showing the isophotal gradient of the combined *g*, *r*, and *i* SDSS filters.
(A color version of this figure is available in the online journal.)

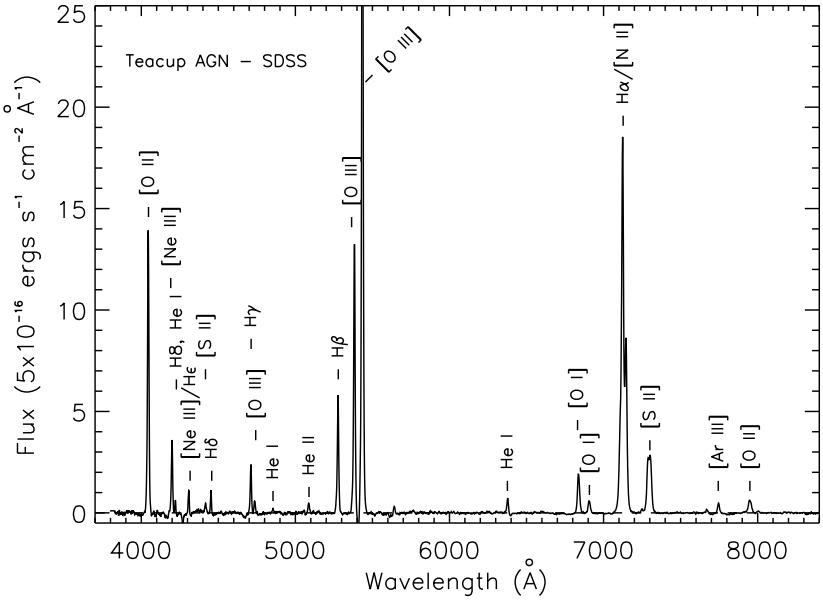

Figure 2. Original SDSS spectrum with prominent lines identified.

opportunity to study the long-term variability of AGNs on timescales of $\leqslant 10^5$ yr. In Section 2 we describe our methods for data acquisition and reduction. In Section 3 we explain our analysis of the data, yielding dereddend line ratios. Our observational results are presented in Section 4, including kinematics of the Teacup AGN as well as FIRST radio data from VLA. In Section 5 we describe our process in creating photoionization models for the Teacup, and review the implications of these models. In Section 6 we discuss our major findings and conclusions.

2. OBSERVATIONS AND DATA REDUCTION

We obtained our primary spectroscopic observations on clear nights at Lowell Observatory's Perkins 1.8 m reflector near Flagstaff, Arizona. We obtained two-dimensional long-slit spectra with the DeVeny "blue" spectrograph with a 300 line mm^{-1} grating, a slit of 2″ width positioned north-south, and a spectral resolution of $\Delta\lambda \approx 3.0$ Å, with R ranging from 1400–2500, between 4300–7600 Å. A total of nine long-slit observations were obtained at six parallel positions relative to the galactic center to cover the 12″ × 12″ field containing the Teacup AGN. Four observations were made at the optical center; for these observations, we averaged the line ratios, and the standard deviation between these four data sets yielded our errors. Three observations were taken moving eastward of the optical center at offset positions of 2″, 4″, and 5″ in order to obtain spectra across the Teacup's ionized "handle," with the last two positions overlapping by 1″. Two more observations

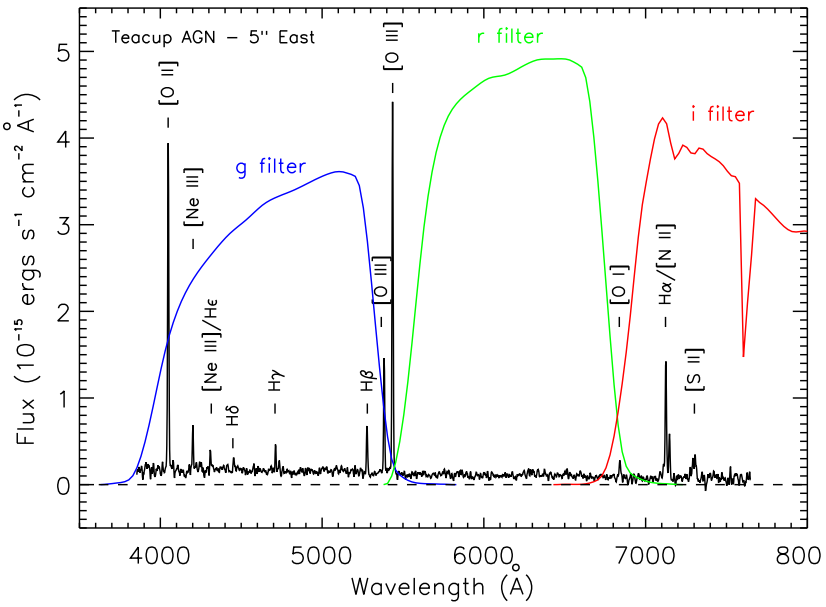

Figure 3. Spectrum taken from Lowell Observatory at 5″ east from the nucleus. Over plotted are the *g*, *r* and *i* SDSS filters. Note [O III] λ 5007 falls directly between the *g* and *r* bandpasses making the Teacup handle appear purple.

(A color version of this figure is available in the online journal.)

were made at 2″ and 4″ west of the optical center. Because of differences in grating positioning in the DeVeny spectrograph, only data from slit positions 5″ east of nucleus and nuclear center (0″) extend into the blue enough to capture [O II] λ3727.

Additionally, we obtained long-slit spectra from the 2.1 m telescope under clear conditions at the Kitt Peak National Observatory and 3.0 m Shane telescope at the Lick Observatory. At KPNO we used the GoldCam spectrograph with the "26new" grating which is a 600 line mm^{-1} grating with $\Delta\lambda \approx 3.3$ Å resolution. This 2″ wide long-slit spectrometer was given a position angle of 37° to capture the top side of the Teacup's "handle" feature. Data collected from the Lick observatory was obtained with the Kast Double Spectrograph, which was set to a 2″ slit width and position angle of 95° covering the bottom side of the ionized "handle." To achieve the correct wavelength coverage we used the 600/7500 and 600/4310 grisms for the red and blue channels, respectively.

Figure 4 shows the vertical 2″ slit positions from Lowell divided into 31 2″ × 2″ extraction bins. Overplotted are the KPNO slit (position angle 37°) and the slit from Lick Observatory (position angle of 95°); see also Keel et al. 2012a. Lastly, data from the VLA FIRST survey (Becker et al. 1995) were analyzed in order to gain a radio luminosity and classification of this object. Table 1 gives a full account of all optical observations including that from SDSS. We reduced our optical data two-dimensionally using IRAF,[10] as well as the NOAO and CTIO packages, resulting in wavelength calibrated spectral images in flux units.

Two-dimensional reduction allowed us to extract multiple spectra in the cross-dispersion direction for each offset slit position in the dispersion direction. While the width of the extraction bin is constrained to 2″ by the slit width, we had the ability to sample our data in the cross-dispersion direction in either 1″ or 2″ bins. Extracting spectra in this manner from each of our six slit positions yielded a total of 62 or 31 individual spectra in 2″ × 1″ (3.4 kpc × 1.7 kpc) or 2″ × 2″ (3.4 kpc × 3.4 kpc) bins, respectively. Spectra sampled in the 2″ × 1″ bins have a higher spatial resolution but a lower signal-to-noise ratio than the data sampled in the 2″ × 2″ bins. Therefore, our signal-to-noise requirements dictated when we could use data binned in the 2″ × 1″ or data in the 2″ × 2″ bins.

To ensure the quality of our data, we required that the fluxes of the important emission lines for each type of analysis have signal-to-noise ratios 3σ. In the case of our kinematic analysis, the emission line of interest is [O III] λ5007, because it is the strongest emission line in our spectra. The strength of [O III] λ5007 allowed us to use the 2″ × 1″ bins to obtain better spatial resolution for our kinematic measurements. For photoionization modeling, the lines of interest were the blended [S II] λλ 6716, 6731 doublet, to obtain accurate densities. This feature is much weaker than the [O III] λ5007, so we used the 2″ × 2″ bins. In the case of the 2″ × 2″ bins, three low signal-to-noise bins from the 4″ west slit were discarded, leaving 28 bins with acceptable signal-to-noise for the majority of our analysis. The seeing for the long-slit spectroscopy was between 1″ and 2″ (FWHM of the point spread function), so some of the kinematics measurements could have been oversampled by up to a factor of two in the spatial direction.

As the spectrum from SDSS has a larger aperture, greater wavelength coverage, and better signal-to-noise than the rest of our observations, we matched the absolute flux as a function of wavelength from SDSS to that of our central extracted bin from Lowell, in order to correct for atmospheric (including refraction) losses. We applied this normalization to the rest of the data for each night before analysis of emission line fluxes for each bin.

3. ANALYSIS

The series of bins allowed us to create a grid of spatially resolved spectra covering the entire galaxy. We analyzed the reduced data utilizing IDL. For each spectral bin we measured emission line fluxes for every non-blended line with a linear

[10] IRAF is distributed by the National Optical Astronomy Observatories, which are operated by the Association of Universities for Research in Astronomy, Inc., under contract with the National Science Foundation.

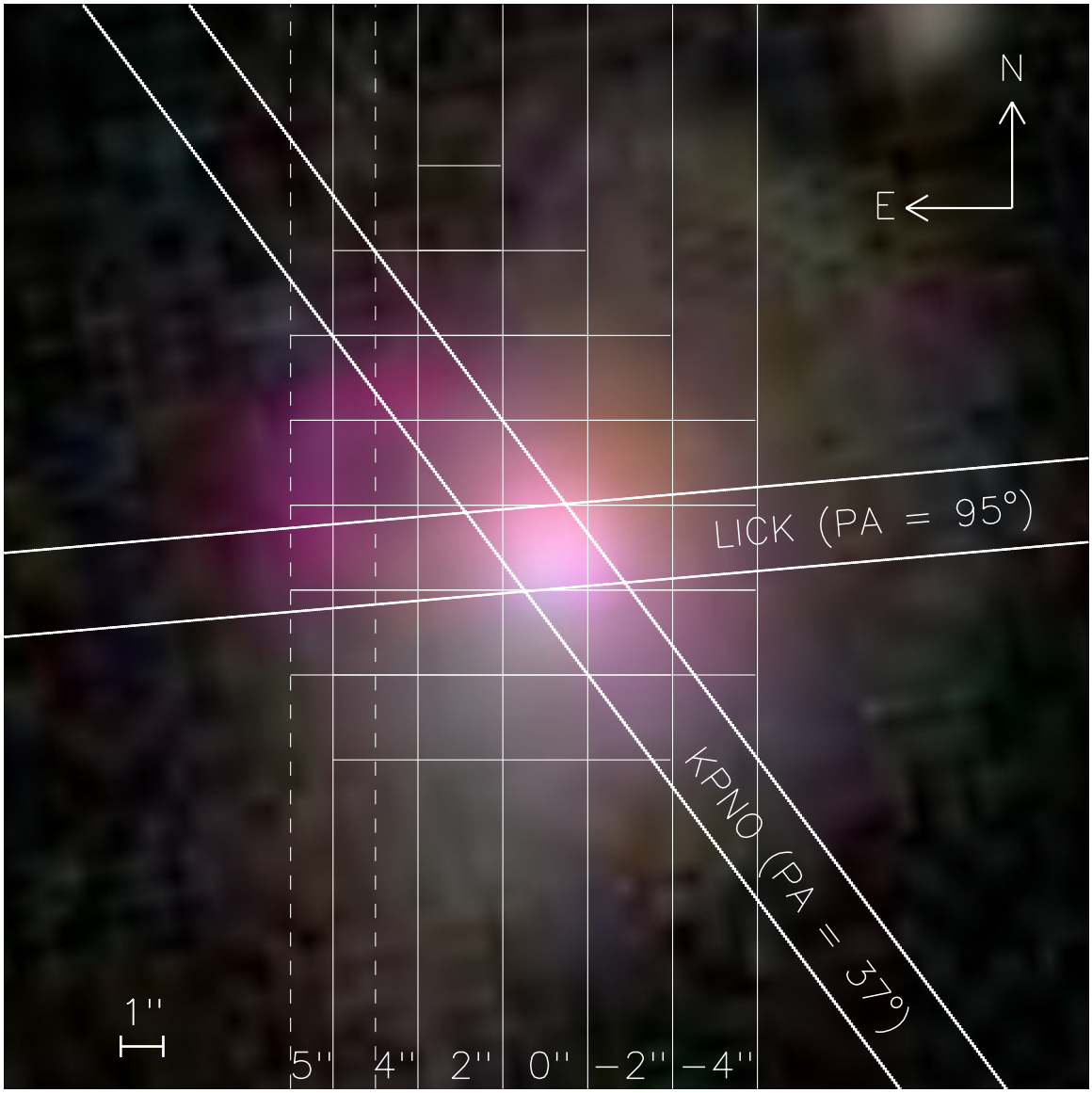

Figure 4. SDSS optical image including slit positions for each observation. The Kast spectrograph position angle can be seen at 95° relative to the north–south axis of the galaxy, and KPNO's GoldCam spectrometer positioned at 37°. The vertical lines represent the different offset positions taken with the Perkins 1.8 m telescope and DeVeny spectrograph. Each extracted bin in the cross-dispersion direction is shown by the horizontal lines crossing each offset position.
(A color version of this figure is available in the online journal.)

Table 1
Observation List for the Teacup AGN

Date	Observatory	Telescope	P.A.	Slit Position from Nucleus	Exposure Time (s)	Wavelength Coverage (Å)
2005 May 13	SDSS	Survey 2.5 m	0°	Center	2880	3800–9250
2009 Apr 18	Lowell	Perkins 1.8 m	0°	Center	1200	3860–7650
2009 Apr 18	Lowell	Perkins 1.8 m	0°	5″ East	1200	3860–7650
2010 May 20	Lowell	Perkins 1.8 m	0°	Center	1200	3870–7660
2010 Jun 15	KPNO	2.1 m	37°	Center	2700	3270–5710
2010 Jul 16	LICK	Shane 3.0 m	95°	Center	1800	3500–5600
2010 Jul 16	LICK	Shane 3.0 m	95°	Center	1800	5540–8340
2011 May 3	Lowell	Perkins 1.8 m	0°	Center	1800	3930–7730
2011 May 3	Lowell	Perkins 1.8 m	0°	2″ West	1800	3930–7730
2011 May 3	Lowell	Perkins 1.8 m	0°	4″ West	1800	3930–7730
2011 May 5	Lowell	Perkins 1.8 m	0°	Center	1800	3930–7730
2011 May 5	Lowell	Perkins 1.8 m	0°	2″ East	1800	3930–7730
2011 May 5	Lowell	Perkins 1.8 m	0°	4″ East	1800	3930–7730

Table 2
$E(B-V)$ and Hβ Flux by Position

Position (x'', y'')	$E(B-V)$ (mag)	Hβ Flux (erg s^{-1} cm^{-2})
(5, 4)	0.17 ± 0.14	1.21×10^{-15} (± 0.21)
(5, 2)	0.00 ± 0.37	1.78×10^{-15} (± 0.23)
(5, 0)	0.00 ± 0.31	1.54×10^{-15} (± 0.42)
(5, −2)	0.11 ± 0.47	0.57×10^{-15} (± 0.16)
(4, 6)	0.16 ± 0.14	0.67×10^{-15} (± 0.09)
(4, 4)	0.21 ± 0.16	1.40×10^{-15} (± 0.19)
(4, 2)	0.21 ± 0.19	1.63×10^{-15} (± 0.16)
(4, 0)	0.40 ± 0.15	1.50×10^{-15} (± 0.16)
(4, −2)	0.35 ± 0.24	0.90×10^{-15} (± 0.16)
(4, −4)	0.27 ± 0.18	0.38×10^{-15} (± 0.13)
(2, 8)	0.14 ± 0.19	0.36×10^{-15} (± 0.12)
(2, 6)	0.03 ± 0.18	1.15×10^{-15} (± 0.18)
(2, 4)	0.22 ± 0.14	2.47×10^{-15} (± 0.30)
(2, 2)	0.35 ± 0.10	4.40×10^{-15} (± 0.44)
(2, 0)	0.53 ± 0.08	3.97×10^{-15} (± 0.30)
(2, −2)	0.60 ± 0.15	2.03×10^{-15} (± 0.31)
(2, −4)	0.43 ± 0.29	0.76×10^{-15} (± 0.18)
(0, 6)	0.04 ± 0.29	1.11×10^{-15} (± 0.33)
(0, 4)	0.43 ± 0.20	2.08×10^{-15} (± 1.21)
(0, 2)	0.62 ± 0.11	6.82×10^{-15} (± 1.84)
(0, 0)	0.53 ± 0.10	12.72×10^{-15} (± 3.02)
(0, −2)	0.41 ± 0.13	4.76×10^{-15} (± 0.44)
(0, −4)	0.26 ± 0.20	0.90×10^{-15} (± 0.27)
(−2, 4)	0.70 ± 0.17	1.21×10^{-15} (± 0.21)
(−2, 2)	0.40 ± 0.09	6.08×10^{-15} (± 0.62)
(−2, 0)	0.26 ± 0.07	7.91×10^{-15} (± 0.52)
(−2, −2)	0.43 ± 0.15	2.94×10^{-15} (± 0.43)
(−2, −4)	0.66 ± 0.22	0.57×10^{-15} (± 0.11)

interpolation procedure that integrates under each line and above a baseline which connects the adjacent continua. For the blended lines of [N II] λλ6548, 6583, and Hα, and the [S II] λλ6716, 6731 doublet, we took a template from the [O III] λ5007 profile and reproduced it at the positions of the blended components simultaneously. By scaling the template up and down it was possible to find a scaling factor for each line relative to [O III]. To determine good fits between the templates and blended lines, we subtracted the scaled components to look at the residuals, rescaling until the residuals were close to the established continuum ensuring good fits (Crenshaw & Peterson 1986). All continuum-subtracted fluxes were then divided by their corresponding Hβ fluxes in order to gain normalized spectral ratios. Reddening, $E(B-V)$, for each $2'' \times 2''$ bin was found by taking Hα/Hβ = 2.9, appropriate for recombination (Osterbrock & Ferland 2006). To calculate the reddening across the entire spectral range for each emission line and correct each spectrum, we used a standard Galactic reddening curve described by Cardelli et al. (1989). As shown in Crenshaw et al. (2001), reddening curves do not differ much in this region of the spectrum and any of a number of curves will provide a reasonable correction to the observed NLR line ratios.

The values of all measured Hβ fluxes and $E(B-V)$ values are listed by position in arcseconds relative to the nucleus in Table 2. Extracted positions listed in each table are given a Cartesian coordinate, where x corresponds to east (positive) and west (negative) positions relative to the nuclear center, and y corresponds to the north (positive) and south (negative) directions. Following this convention, the nuclear center is labeled as (0″, 0″). The resultant normalized and dereddened line ratios can be found in Tables 3 and 4.

We attribute the uncertainties in our flux measurements to a combination of photon noise (propagated through the data reduction process), measurement errors (including placement of the continuum), and errors in the reddening correction (propagated from the lines used to determine the reddening). To constrain our errors in measurement, we performed the same flux measurement procedure three times on each line with different reasonable continuum placements and found the standard deviation. The leading source of error in our reddening correction is from our errors associated with the measured Hβ fluxes, as the Hα/Hβ ratio was employed to determine $E(B-V)$. These sources of error were all summed in quadrature, resulting in our final dereddened line ratio errors.

Dereddened normalized fluxes were employed in several diagnostic tests using "BPT" diagrams as shown in Figure 5 (Baldwin et al. 1981). According to these diagrams adopted from Kewley et al. (2006), our emission line ratios indicate that the Teacup AGN is indeed a Seyfert 2 undergoing photoionization from a central ionizing source. There is no evidence from these diagrams for a strong contribution from starbursts to the ionizing radiation.

Because of the relative strength of the [O III] λ5007 emission line we were able to employ our $2'' \times 1''$ bins to map out [O III] flux and kinematics, as well as include the bins located at 4″ west. To probe large-scale motions of the ionized gas in this galaxy, kinematics were determined by fitting Gaussians to the [O III] λ5007 lines (see Fischer et al. 2010) and determining their central wavelengths for all 62 bins spanning a 20.4 kpc × 28.9 kpc field. These wavelengths were converted to velocity offsets from the rest frame of the galaxy, defined in this case by the velocity of our centrally extracted bin. Our data do not have high enough signal-to-noise to get a galactic velocity from stellar absorption lines. The data from the KPNO and Lick observatories provided us with additional two-dimensional spectra which allowed us to investigate the kinematics of the ionized loop of gas protruding from the nucleus of the object. The FWHM([O III]) was also measured for each Lowell bin; the instrumental FWHM was subtracted off these values in quadrature to obtain the intrinsic FWHM.

4. OBSERVATIONAL RESULTS

Having mapped out the Teacup with spatially resolved spectra, we were able to investigate the emission line reddening, fluxes, and kinematics in a grid over our object. Figure 6 shows a map of measured $E(B-V)$ reddening values per location on the left-hand side. The regions around (0″, 2″) and (−2″, 4″) show the highest levels of reddening. The reddening map suggests a possible dust lane running southeast to northwest at PA ≈ −45°. Figure 6 also shows [O III] λ5007 flux for each $2''$ × $2''$ bin, measured in terms of erg s^{-1} cm^{-2}. The position (0″, 0″) shows the largest [O III] flux of 9.7×10^{-14} erg s^{-1} cm^{-2} at the location of the nucleus.

Our [O III] velocity map, presented on the left in Figure 7, shows the NE region of the ionized handle at position (2″, 9″) receding with a maximum redshifted velocity of 150 km s^{-1} relative to the center of the galaxy, while the position (−4″, −2″) has the largest blueshifted velocity of 340 km s^{-1}. The velocity pattern shows a clear kinematic axis running SE to NW with a low range in radial velocities, indicative of rotational motion. Considering the region sampled hosts a majority of the galaxy, the observed kinematics must be due primarily to galactic rotation. This places the axis of rotation at P.A. ≈ −50°. The panel of Figure 7 shows measured FWHM values in terms

Table 3
Dereddend Line Ratios (λ3727–λ4686)[a,b]

Position (x'', y'')	[O II] λ3727	[Ne III] λ3869	H8,He I λ3889	Hϵ, [Ne III] λ3970	Hδ λ4100 λ4100	Hγ λ4341	[O III] λ4363	He II λ4686
(5, 4)	10.07 ± 1.25	1.19 ± 0.13	···	0.45 ± 0.04	···	0.60 ± 0.04	···	···
	(7.28)	(0.76)	(0.19)	(0.39)	(0.26)	(0.47)	(0.07)	(0.42)
(5, 2)	8.00 ± 1.48	0.96 ± 0.16	0.25 ± 0.04	0.34 ± 0.05	0.19 ± 0.02	0.41 ± 0.04	0.14 ± 0.01	0.25 ± 0.01
	(7.28)	(0.76)	(0.19)	(0.39)	(0.26)	(0.47)	(0.07)	(0.42)
(5, 0)	8.17 ± 2.23	0.88 ± 0.21	0.20 ± 0.05	0.31 ± 0.07	···	0.38 ± 0.05	···	···
	(7.37)	(0.65)	(0.21)	(0.35)	(0.26)	(0.47)	(0.05)	(0.14)
(5, −2)	9.99 ± 4.18	1.41 ± 0.51	···	0.93 ± 0.30	···	0.90 ± 0.18	···	···
	(7.08)	(0.70)	(0.19)	(0.37)	(0.26)	(0.47)	(0.06)	(0.34)
(4, 6)	···	1.08 ± 0.11	···	0.51 ± 0.05	0.23 ± 0.02	0.58 ± 0.03	···	···
	(7.31)	(0.76)	(0.19)	(0.39)	(0.26)	(0.47)	(0.07)	(0.42)
(4, 4)	···	0.98 ± 0.12	···	0.47 ± 0.05	0.38 ± 0.04	0.37 ± 0.03	0.10 ± 0.01	···
	(6.06)	(0.83)	(0.20)	(0.41)	(0.26)	(0.47)	(0.10)	(0.14)
(4, 2)	···	1.01 ± 0.15	···	0.50 ± 0.07	0.20 ± 0.02	0.65 ± 0.05	0.21 ± 0.02	···
	(5.11)	(0.68)	(0.20)	(0.36)	(0.26)	(0.47)	(0.06)	(0.19)
(4, 0)	···	1.07 ± 0.12	···	0.54 ± 0.06	0.20 ± 0.02	0.45 ± 0.03	0.15 ± 0.01	0.16 ± 0.003
	(5.11)	(0.68)	(0.20)	(0.36)	(0.26)	(0.47)	(0.06)	(0.19)
(4, −2)	···	1.12 ± 0.20	···	···	···	0.49 ± 0.05	···	···
	(4.25)	(0.60)	(0.18)	(0.34)	(0.26)	(0.47)	(0.06)	(0.48)
(4, −4)	···	0.45 ± 0.06	···	···	···	···	···	···
	(4.30)	(0.52)	(0.21)	(0.32)	(0.26)	(0.47)	(0.03)	(0.14)
(2, 8)	···	1.30 ± 0.18	···	···	···	···	···	···
	(4.25)	(0.61)	(0.18)	(0.35)	(0.26)	(0.47)	(0.06)	(0.47)
(2, 6)	···	0.88 ± 0.12	···	0.38 ± 0.05	···	0.56 ± 0.04	···	0.12 ± 0.003
	(4.31)	(0.61)	(0.20)	(0.34)	(0.26)	(0.47)	(0.05)	(0.31)
(2, 4)	···	0.91 ± 0.10	0.27 ± 0.03	0.30 ± 0.03	0.25 ± 0.02	0.42 ± 0.03	0.11 ± 0.01	0.11 ± 0.002
	(7.36)	(0.69)	(0.20)	(0.37)	(0.26)	(0.47)	(0.04)	(0.22)
(2, 2)	···	0.79 ± 0.06	···	0.23 ± 0.02	0.20 ± 0.01	0.44 ± 0.02	0.10 ± 0.004	0.12 ± 0.002
	(10.06)	(0.82)	(0.15)	(0.39)	(0.24)	(0.46)	(0.18)	(0.15)
(2, 0)	···	0.85 ± 0.05	···	0.22 ± 0.01	0.25 ± 0.01	0.45 ± 0.02	0.19 ± 0.01	0.16 ± 0.002
	(5.11)	(0.68)	(0.20)	(0.36)	(0.26)	(0.47)	(0.06)	(0.19)
(2, −2)	···	1.25 ± 0.14	···	0.14 ± 0.01	0.14 ± 0.01	···	···	0.09 ± 0.002
	(5.11)	(0.68)	(0.20)	(0.36)	(0.26)	(0.47)	(0.06)	(0.19)
(2, −4)	···	0.64 ± 0.14	···	···	···	···	···	···
	(8.70)	(0.75)	(0.13)	(0.37)	(0.24)	(0.46)	(0.14)	(0.38)
(0, 6)	···	0.79 ± 0.18	···	0.42 ± 0.09	···	0.39 ± 0.05	···	···
	(10.44)	(0.72)	(0.13)	(0.36)	(0.24)	(0.47)	(0.10)	(0.41)
(0, 4)	11.02 ± 1.86	1.15 ± 0.17	···	0.37 ± 0.05	0.33 ± 0.04	0.51 ± 0.04	0.17 ± 0.01	0.15 ± 0.004
	(10.15)	(0.85)	(0.13)	(0.40)	(0.26)	(0.46)	(0.16)	(0.38)
(0, 2)	9.31 ± 0.83	1.22 ± 0.10	0.24 ± 0.02	0.34 ± 0.02	0.22 ± 0.01	0.63 ± 0.03	0.19 ± 0.01	···
	(7.04)	(0.94)	(0.19)	(0.45)	(0.26)	(0.47)	(0.12)	(0.42)
(0, 0)	6.22 ± 0.52	0.91 ± 0.07	0.27 ± 0.02	0.24 ± 0.02	0.18 ± 0.01	0.48 ± 0.02	0.12 ± 0.01	···
	(6.17)	(0.83)	(0.19)	(0.41)	(0.26)	(0.47)	(0.09)	(0.04)
(0, −2)	8.01 ± 0.91	1.07 ± 0.11	0.22 ± 0.02	0.25 ± 0.02	0.21 ± 0.02	0.55 ± 0.03	0.17 ± 0.01	···
	(8.70)	(0.75)	(0.13)	(0.37)	(0.24)	(0.46)	(0.14)	(0.38)
(0, −4)	11.74 ± 2.20	1.43 ± 0.23	0.23 ± 0.04	···	···	0.60 ± 0.06	···	···
	(8.70)	(0.75)	(0.13)	(0.37)	(0.24)	(0.46)	(0.14)	(0.38)
(−2, 4)	···	0.85 ± 0.11	···	···	···	···	···	···
	(4.26)	(0.63)	(0.19)	(0.35)	(0.26)	(0.47)	(0.06)	(0.37)
(−2, 2)	···	0.85 ± 0.06	···	0.17 ± 0.01	0.11 ± 0.01	0.45 ± 0.02	···	···
	(6.03)	(0.82)	(0.19)	(0.41)	(0.26)	(0.47)	(0.09)	(0.37)
(−2, 0)	···	0.72 ± 0.04	···	0.23 ± 0.01	0.12 ± 0.005	0.40 ± 0.01	···	···
	(10.08)	(0.78)	(0.13)	(0.38)	(0.24)	(0.47)	(0.13)	(0.43)
(−2, −2)	···	0.76 ± 0.09	···	0.27 ± 0.03	···	0.41 ± 0.03	···	···
	(10.13)	(0.72)	(0.13)	(0.36)	(0.24)	(0.46)	(0.09)	(0.38)
(−2, −4)	···	1.79 ± 0.30	···	···	···	···	···	···
	(8.37)	(0.80)	(0.12)	(0.38)	(0.24)	(0.47)	(0.18)	(0.43)

Notes.
[a] Model values are given in parentheses.
[b] Positions presented in Cartesian format (x, y), with positive x values for east of center and negative for west. By the same format, positive y denotes north of center and negative for south. The center position is marked by (0, 0).

Table 4
Dereddend Line Ratios (λ4959–λ6731)[a]

Position (x'', y'')	[O III] λ4959	[O III] λ5007	He I λ5876	[O I] λ6300	[O I] λ6364	[N II] λ6548	[N II] λ6583	[S II] λ6716	[S II] λ6731
(5, 4)	2.64 ± 0.03	8.33 ± 0.13	...	0.36 ± 0.05	...	0.35 ± 0.05	1.20 ± 0.19	0.49 ± 0.08	0.56 ± 0.09
	(2.55)	(7.68)	(0.09)	(0.21)	(0.07)	(0.55)	(1.63)	(0.89)	(0.88)
(5, 2)	2.13 ± 0.03	7.10 ± 0.16	...	0.40 ± 0.08	...	0.30 ± 0.07	1.12 ± 0.27	0.52 ± 0.13	0.59 ± 0.15
	(2.55)	(7.68)	(0.09)	(0.21)	(0.07)	(0.55)	(1.63)	(0.89)	(0.88)
(5, 0)	2.09 ± 0.04	6.77 ± 0.22	...	0.29 ± 0.09	...	0.41 ± 0.14	1.15 ± 0.40	0.68 ± 0.25	0.54 ± 0.20
	(2.03)	(6.11)	(0.13)	(0.21)	(0.07)	(0.55)	(1.62)	(0.93)	(0.87)
(5, −2)	2.17 ± 0.07	7.17 ± 0.36	...	0.59 ± 0.27	...	0.27 ± 0.14	0.97 ± 0.53	...	...
	(2.24)	(6.75)	(0.10)	(0.58)	(0.18)	(0.57)	(1.67)	(1.19)	(1.11)
(4, 6)	2.35 ± 0.02	8.16 ± 0.12	...	...	...	0.29 ± 0.04	1.13 ± 0.17	0.63 ± 0.10	0.63 ± 0.10
	(2.64)	(7.93)	(0.09)	(0.08)	(0.03)	(0.53)	(1.56)	(0.76)	(0.77)
(4, 4)	2.55 ± 0.03	7.73 ± 0.13	...	0.44 ± 0.07	...	0.29 ± 0.05	1.13 ± 0.20	0.69 ± 0.13	0.61 ± 0.12
	(3.11)	(9.36)	(0.12)	(0.49)	(0.16)	(0.43)	(1.27)	(0.86)	(0.79)
(4, 2)	2.67 ± 0.03	7.78 ± 0.16	...	0.50 ± 0.09	...	0.39 ± 0.08	1.07 ± 0.23	0.60 ± 0.14	0.60 ± 0.14
	(2.59)	(7.80)	(0.12)	(0.36)	(0.12)	(0.43)	(1.26)	(0.76)	(0.76)
(4, 0)	2.72 ± 0.03	7.53 ± 0.12	...	0.38 ± 0.05	...	0.34 ± 0.06	0.96 ± 0.16	0.59 ± 0.11	0.62 ± 0.11
	(2.59)	(7.80)	(0.12)	(0.36)	(0.12)	(0.43)	(1.26)	(0.76)	(0.76)
(4, −2)	2.01 ± 0.03	6.53 ± 0.17	...	0.43 ± 0.10	...	0.35 ± 0.09	1.14 ± 0.31	0.54 ± 0.15	0.70 ± 0.20
	(2.16)	(6.51)	(0.09)	(0.29)	(0.09)	(0.45)	(1.33)	(0.65)	(0.78)
(4, −4)	1.27 ± 0.02	5.40 ± 0.10	...	...	...	0.35 ± 0.07	1.15 ± 0.22	...	...
	(1.83)	(5.50)	(0.13)	(0.29)	(0.09)	(0.45)	(1.34)	(0.65)	(0.79)
(2, 8)	1.76 ± 0.02	6.19 ± 0.12	...	...	...	0.33 ± 0.07	1.45 ± 0.30	0.69 ± 0.15	0.85 ± 0.19
	(2.24)	(6.73)	(0.09)	(0.29)	(0.09)	(0.45)	(1.33)	(0.65)	(0.78)
(2, 6)	2.03 ± 0.02	6.64 ± 0.13	...	0.28 ± 0.05	...	0.39 ± 0.08	1.16 ± 0.23	0.65 ± 0.14	0.77 ± 0.16
	(2.22)	(6.67)	(0.11)	(0.47)	(0.15)	(0.47)	(1.38)	(0.80)	(0.90)
(2, 4)	2.35 ± 0.02	7.46 ± 0.11	0.10 ± 0.01	0.41 ± 0.06	0.16 ± 0.02	0.44 ± 0.07	1.20 ± 0.19	0.64 ± 0.11	0.59 ± 0.10
	(2.26)	(6.82)	(0.12)	(0.21)	(0.07)	(0.55)	(1.62)	(0.93)	(0.87)
(2, 2)	2.33 ± 0.02	7.19 ± 0.08	0.15 ± 0.01	0.42 ± 0.04	0.08 ± 0.01	0.39 ± 0.04	1.22 ± 0.14	0.59 ± 0.07	0.49 ± 0.06
	(2.49)	(7.50)	(0.07)	(0.41)	(0.13)	(0.41)	(1.21)	(1.03)	(0.82)
(2, 0)	2.47 ± 0.01	7.80 ± 0.07	0.10 ± 0.01	0.35 ± 0.03	0.09 ± 0.01	0.35 ± 0.03	1.19 ± 0.11	0.48 ± 0.05	0.44 ± 0.04
	(2.59)	(7.80)	(0.12)	(0.36)	(0.12)	(0.43)	(1.26)	(0.76)	(0.76)
(2, −2)	2.41 ± 0.02	7.81 ± 0.13	...	0.63 ± 0.05	...	0.35 ± 0.06	1.16 ± 0.20	0.54 ± 0.10	0.50 ± 0.09
	(2.59)	(7.80)	(0.12)	(0.36)	(0.12)	(0.43)	(1.26)	(0.76)	(0.76)
(2, −4)	2.35 ± 0.05	8.24 ± 0.26	...	0.60 ± 0.17	...	0.49 ± 0.16	1.45 ± 0.48	0.68 ± 0.24	0.54 ± 0.19
	(2.50)	(7.54)	(0.04)	(0.51)	(0.16)	(0.35)	(1.03)	(0.98)	(0.78)
(0, 6)	1.77 ± 0.04	5.47 ± 0.17	...	0.35 ± 0.10	...	0.42 ± 0.14	1.16 ± 0.38	0.68 ± 0.24	0.55 ± 0.19
	(2.07)	(6.23)	(0.04)	(0.40)	(0.13)	(0.41)	(1.22)	(0.98)	(0.84)
(0, 4)	2.17 ± 0.03	7.40 ± 0.15	0.09 ± 0.01	0.39 ± 0.07	...	0.42 ± 0.09	1.34 ± 0.29	0.56 ± 0.13	0.53 ± 0.12
	(2.71)	(8.16)	(0.04)	(0.42)	(0.14)	(0.39)	(1.15)	(0.99)	(0.79)
(0, 2)	2.70 ± 0.02	8.34 ± 0.09	0.10 ± 0.01	0.45 ± 0.04	...	0.46 ± 0.05	1.33 ± 0.15	0.42 ± 0.05	0.39 ± 0.05
	(3.45)	(10.39)	(0.09)	(0.28)	(0.09)	(0.49)	(1.45)	(0.79)	(0.81)
(0, 0)	2.56 ± 0.02	7.64 ± 0.08	0.11 ± 0.01	0.34 ± 0.03	...	0.44 ± 0.05	1.29 ± 0.14	0.43 ± 0.05	0.39 ± 0.04
	(3.16)	(9.50)	(0.10)	(0.28)	(0.09)	(0.46)	(1.35)	(0.79)	(0.77)
(0, −2)	2.66 ± 0.02	8.29 ± 0.12	0.12 ± 0.01	0.45 ± 0.06	...	0.45 ± 0.06	1.31 ± 0.19	0.52 ± 0.08	0.43 ± 0.07
	(2.50)	(7.54)	(0.04)	(0.51)	(0.16)	(0.35)	(1.03)	(0.98)	(0.78)
(0, −4)	2.58 ± 0.04	7.71 ± 0.18	...	0.49 ± 0.10	...	0.47 ± 0.11	1.33 ± 0.32	0.54 ± 0.14	0.42 ± 0.11
	(2.50)	(7.71)	(0.04)	(0.51)	(0.16)	(0.35)	(1.03)	(0.98)	(0.78)
(−2, 4)	1.94 ± 0.02	7.26 ± 0.13	...	0.62 ± 0.10	...	0.48 ± 0.09	1.19 ± 0.22	0.37 ± 0.07	0.40 ± 0.08
	(2.42)	(7.29)	(0.10)	(0.29)	(0.09)	(0.45)	(1.33)	(0.64)	(0.78)
(−2, 2)	2.98 ± 0.02	9.13 ± 0.09	...	0.47 ± 0.04	...	0.47 ± 0.05	1.41 ± 0.15	0.45 ± 0.05	0.48 ± 0.05
	(3.11)	(9.35)	(0.10)	(0.38)	(0.12)	(0.46)	(1.34)	(0.85)	(0.80)
(−2, 0)	2.47 ± 0.01	7.66 ± 0.06	...	0.38 ± 0.03	...	0.48 ± 0.04	1.42 ± 0.11	0.62 ± 0.05	0.44 ± 0.04
	(2.34)	(7.05)	(0.04)	(0.44)	(0.14)	(0.41)	(1.21)	(0.98)	(0.83)
(−2, −2)	1.86 ± 0.02	6.00 ± 0.10	...	0.46 ± 0.07	...	0.36 ± 0.06	1.21 ± 0.21	0.64 ± 0.12	0.36 ± 0.07
	(2.12)	(6.39)	(0.04)	(0.47)	(0.15)	(0.43)	(1.25)	(1.03)	(0.88)
(−2, −4)	2.18 ± 0.03	7.73 ± 0.18	...	0.55 ± 0.12	...	0.37 ± 0.09	1.04 ± 0.26	1.00 ± 0.26	0.42 ± 0.11
	(2.76)	(8.31)	(0.03)	(0.50)	(0.16)	(0.34)	(0.99)	(0.94)	(0.75.)

Note. [a] Model values are given in parentheses.

of km s^{-1}, for the [O III] λ5007 emission line. In general, the FWHM increases toward the central nucleus, which is also supporting evidence for galactic rotation. However, the dust lane runs along the same direction as the rotational axis, which is certainly not typical for normal disk galaxies, suggesting disturbed kinematics, possibly due to a merger.

Additional kinematic results from both the KPNO 2.1 m and Lick Shane 3 m telescopes agree with this interpretation.

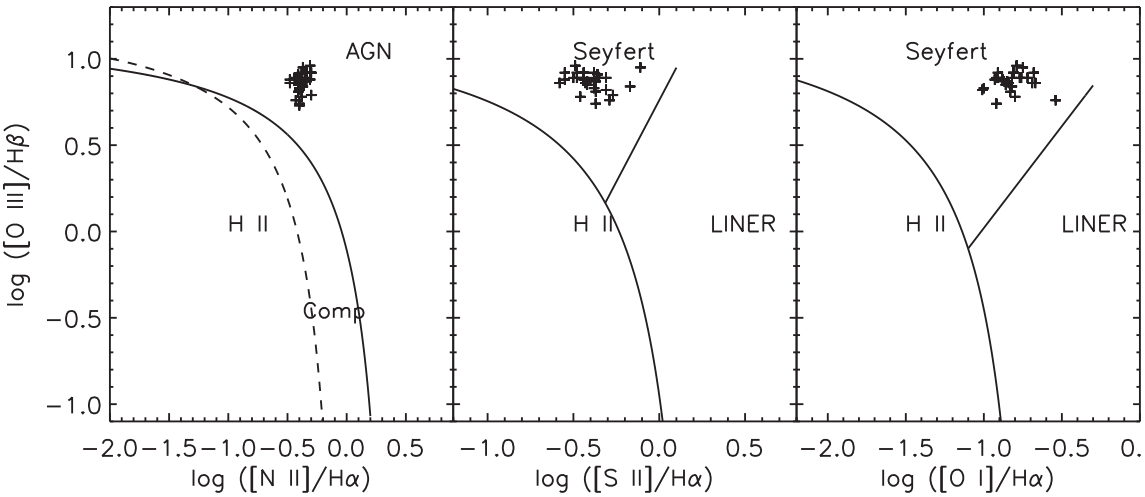

Figure 5. BPT/Kewley diagrams show the Teacup is a type 2 photoionized AGN.

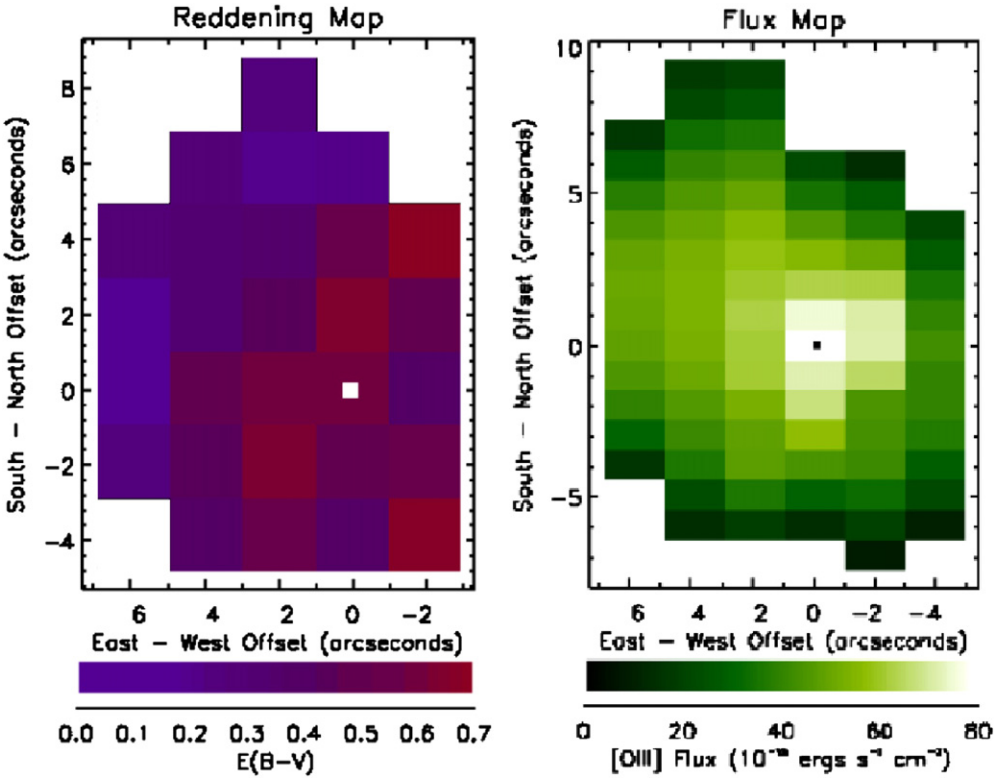

Figure 6. Reddening map (left), binned in $2'' \times 2''$ squares and shows the $E(B-V)$ for each given region. Right: a flux map of the observed [O III] λ 5007 flux in the $2'' \times 1''$ bins.

(A color version of this figure is available in the online journal.)

As these observations were made at different slit position angles, we created a procedure that utilized our grid of Lowell observed velocities to simulate an artificial slit at the KPNO/Lick observation position angles and then extracted the pseudo-slit kinematics. Figure 8 displays radial velocity curves from KPNO at 37° and LICK at 95° as well as our extracted velocity curves from Lowell overplotted. In general, the velocities from the different data sets agree extremely well, and the KPNO and Lick observations allow us to trace the radial velocities out to greater distances. The radial velocity curve from the Lick data turns over from a redshift to a blueshift at around 22″ northeast of the nucleus. This suggests once again that there are other physical phenomena affecting the kinematics at large distances in addition to mere galactic rotation. This turnover is not seen in the velocity map compiled from Lowell, because at 22″ away from the center, it is outside the scope of our Lowell observations. A slight bump in the radial velocity curves at the location of the teacup handle suggests an additional kinematic component at this location, possibly outflow, even though the magnitude is relatively low (∼50 km s^{-1}).

We also investigate the radio properties of the Teacup. Figure 9 shows a 20 cm radio image from the FIRST survey. In the right panel of Figure 9 is the SDSS *g*-band image. The radio emission has a flux of 26.41 ± 0.15 mJy ($4.2 \times {}^{23}$ W Hz^{-1}) and extends along the direction of the "handle". The radio image was deconvolved into two Gaussian components using the routine JMFIT in AIPS. The stronger component, with a flux of 19.28 ± 0.33 mJy, corresponds to the nucleus. The second component,

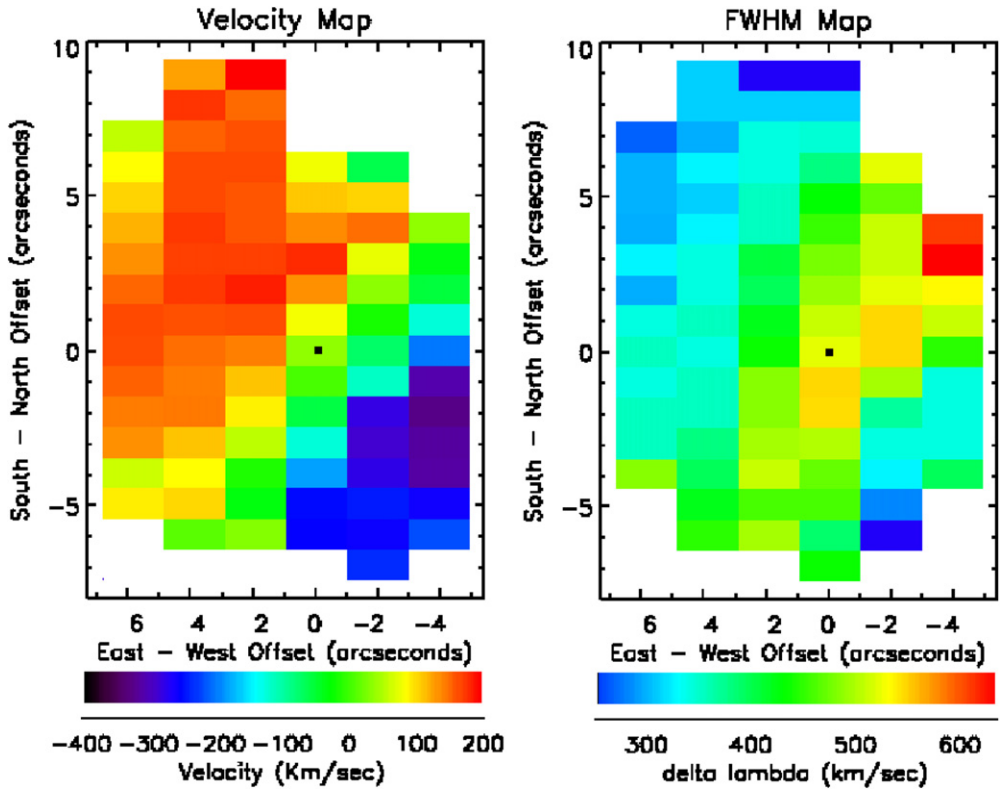

Figure 7. Velocity map (left) shows the velocity of the $2'' \times 1''$ bins relative to the nucleus (marked with a black dot). The map on the right shows measured FWHM values in km s^{-1} in the $2'' \times 1''$ bins. In this and subsequent figures, the $5''$ E position has been offset by an additional $1''$ E for display purposes.
(A color version of this figure is available in the online journal.)

at $6''.1$ from the nucleus, along P.A. $= 74°$, has a flux of 5.86 ± 0.15 mJy. There is a correspondence between the direction of the radio emission and the ionized gas in the handle. The radio luminosity of the Teacup is only 4.2×10^{23} W Hz^{-1}, which is only slightly above the radio-loud dividing line of 1×10^{23} W Hz^{-1} (Best et al. 2005), making the Teacup a radio-intermediate AGN.

5. PHOTOIONIZATION MODELS

5.1. Initial Conditions

To gain physical insight, we generated photoionization models for the Teacup AGN with CLOUDY version 8.00 (see Ferland et al. 1998), which replicates the observed line ratios by modeling a central ionizing source acting upon a gaseous region, in this case modeled with a slab geometry at each position (Kraemer et al. 1994). To satisfy signal-to-noise requirements, we modeled each spectrum extracted from the $2''$ by $2''$ regions (excluding $4''$ west data because of poor signal-to-noise). In order to accurately model the photoionizing conditions of the Teacup, we first had to derive an expression for the spectral energy distribution (SED). Our initial strategy followed from Kraemer et al. (1994), looking at the observed ratio of He IIλ4686 relative to Hβ. We determined the ionizing UV power law index α from

$$R = \frac{Q(\mathrm{H}^0)}{Q(\mathrm{He}^+)} \approx \left(\frac{1}{4}\right)^{\alpha} - 1, \quad (1)$$

where R is the ratio of photons (Q) which are ionizing H^0 and He^+. R can be determined from relative densities (n), intensities (I), and volume emissivities (j) of the two lines in question, along with the dereddened ratio:

$$R = \frac{n(\mathrm{He})}{n(\mathrm{H})} \frac{I(\mathrm{H}\beta)}{I(\mathrm{He\,II}\lambda 4686)} \frac{j(\mathrm{He\,II}\lambda 4686)}{j(\mathrm{H}\beta)}. \quad (2)$$

Using this method for each extracted spectrum we arrived at an initial average index of $\alpha = -1.7$. However, upon inspection of our initial models with this spectral index we found that we were predicting 30% more He II/Hβ than we were observing. For this reason we decreased α to -2.0 which resulted in our models matching He II/Hβ to within ± 10 %. We described our final SED as a piecewise function, similar to that used by our group for other AGNs (Kraemer & Crenshaw 2000):

$$\alpha = -1.0, \quad h\nu < 13.6 \text{ eV}, \quad (3)$$

$$\alpha = -2.0, \quad 13.6 \text{ eV} \quad h\nu < 1000 \text{ eV}, \quad (4)$$

$$\alpha = -1.0, \quad h\nu \quad 1000 \text{ eV}. \quad (5)$$

Previous work by Kraemer & Crenshaw (2000) has demonstrated solar abundances are usually sufficient to accurately model the physical conditions in Seyfert 2 narrow-line regions. Based on this experience solar abundances were employed with and without dust depletion and we found no appreciable difference. Because there is no direct evidence for dust depletions or elemental peculiarities, we assumed solar elemental abundances (Asplund et al. 2005) without dust depletion. The numerical values relative to Hydrogen for these abundances are: He $=$ 0.10, C $= 2.45 \times 10^{-4}$, N $= 6.03 \times 10^{-5}$, O $= 4.57 \times 10^{-4}$, Ne $= 6.92 \times 10^{-5}$, Na $= 2.09 \times 10^{-6}$, Mg $= 3.39 \times 10^{-5}$, Al $= 3.09 \times 10^{-6}$, Si $= 3.24 \times 10^{-5}$, S $= 1.38 \times 10^{-5}$,

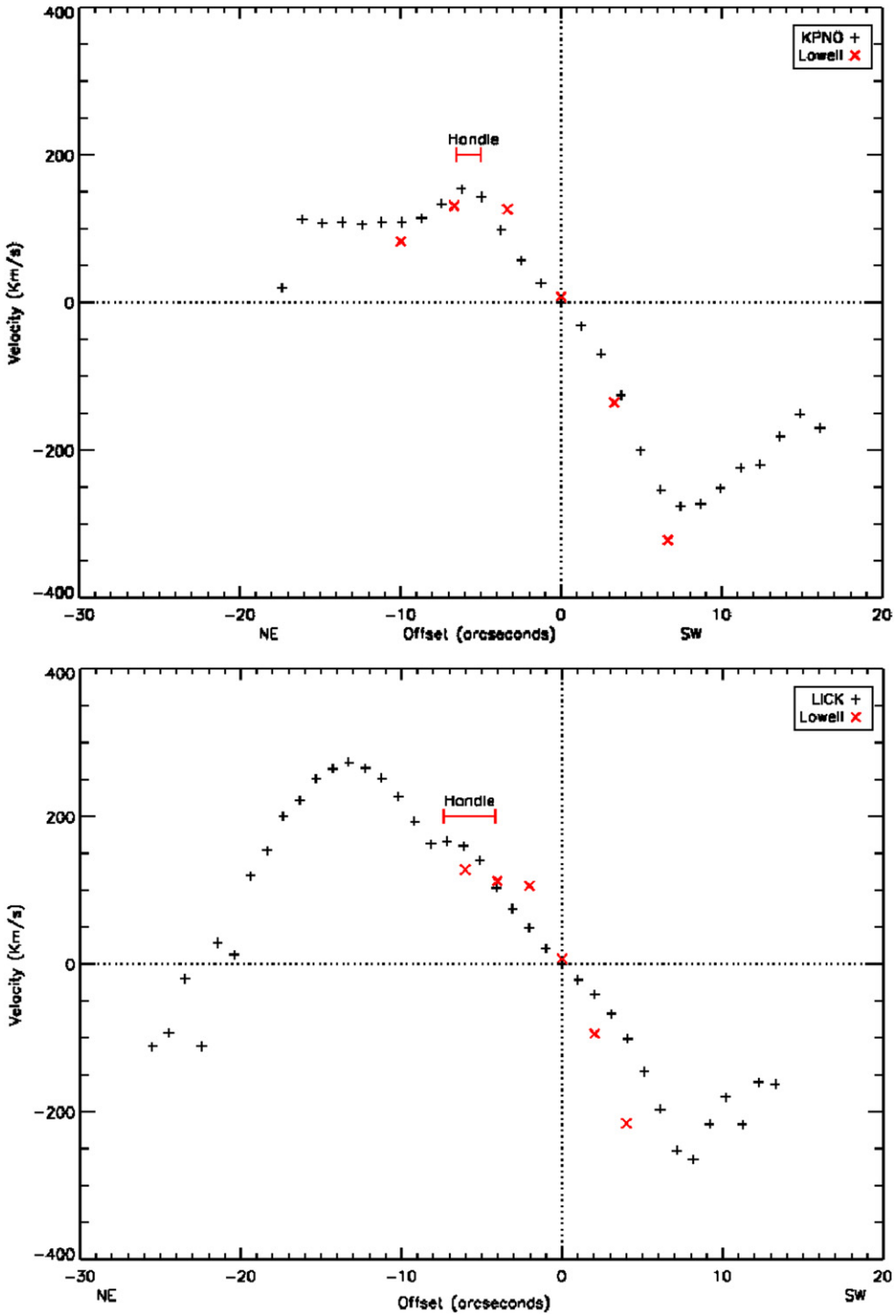

Figure 8. Radial velocities measured from KPNO's 2.1−m telescope at 37° and LICK's 3 m Shane telescope at 95° positions angles relative to the north−south axis. Overplotted are velocities extracted from the Lowell data.

(A color version of this figure is available in the online journal.)

Ar $= 2.51 \times 10^{-6}$, Ca $= 2.24 \times 10^{-6}$, Fe $= 2.82 \times 10^{-5}$, and Ni $= 1.78 \times 10^{-6}$.

By using the ratio of [S II] λλ 6716 to 6731 to estimate the density n_H (Osterbrock & Ferland 2006), our last free parameter is the unitless ionization parameter, U, described by Ferland & Netzer (1983):

$$U = \frac{Q(H^0)}{4\pi r_{\rm AGN}^2 n_H c}, \quad (6)$$

where $Q(H^0)$ is the number of ionizing photons emitted by the source per second, $r_{\rm AGN}$ is the distance from the central source to the ionized cloud, and n_H is the hydrogen density of the gas. We assumed that $r_{\rm AGN}$ is approximately the projected distance from each extracted bin to the ionizing source, in this case simplified to be bin (0″, 0″).

5.2. Model Components and Types

Our initial models consisted of only a single component, with SED and abundances set as described above. For each extracted

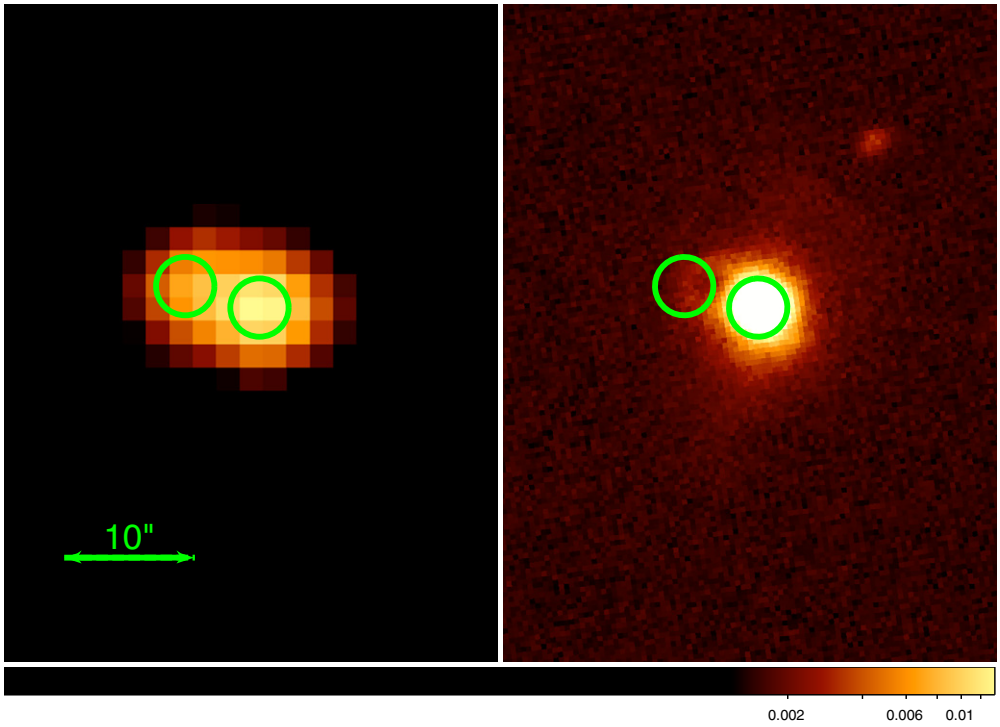

Figure 9. Left: 20 cm Radio FIRST image deconvolved into two Gaussians. Right: SDSS *g*-band image.
(A color version of this figure is available in the online journal.)

position, n_H was set from the ratio of [S II], leaving U and column depth N_H as free parameters. Values of U were then chosen based on specific line intensities such as [O III] λ5007, [N II] λ6584, and [S II] λ6731 given by Ferland & Netzer (1983). Initial values for N_H were chosen to be $\sim 10^{21}$ cm^{-2}, similar to values previously used by Kraemer et al. (2001). Our initial values of U and N_H were then varied until our models fit our data to within a factor of two. Single-component models were sufficient to replicate most of the observed emission lines. However, these models were unable to match the observed intensity of [O II] λ3727 within an acceptable error defined as the ratio of modeled line intensity divided by dereddened observed line intensity, with a good fit having a ratio 2 and a perfect fit with a ratio = 1. As our best single component models underpredicted the [O II] intensity by a factor of three or greater, we included a second component into our CLOUDY models.

Our two-component models consisted of a low-ionization component (log(U) −3.0) and a high-ionization component (log(U) −3.0). The low-ionization component contributes the majority of the emission lines including [O II] λ3727, [O I] λ6300, [N II] λλ6548, 6584, and [S II] λλ 6716, 6731, while the high-ionization component contributes the majority of the [O III] λ5007 emission. Blending the line ratios of both the high- and low-ionization components yields our composite model line intensities, which we compared to our observed dereddened values. Because our spectra are spatially resolved, we had to assure that both the high- and low-ionization components for each model were co-located with the same distance $r_{\rm AGN}$ from the source. From Equation (6), we were able to constrain each co-located set with the condition that $\log(U_{\rm low\ ion}) + \log(n_{H\ \rm low\ ion}) = \log(U_{\rm high\ ion}) + \log(n_{H\ \rm high\ ion})$. However, our two-component models still underpredicted [O II] λ3727 by a factor of ∼3 or more in most cases, forcing us to consider other possible ionizing mechanisms that might boost [O II]. While our BPT diagrams suggest this object is photoionized, we decided to explore the possibilities of shock ionization.

To consider shock ionization, we matched both our observed FWHM values and observed densities to the shock velocities and hydrogen densities used in radiative shock models, generated by Allen et al. (2008), comparing our data only to Allen's models with solar abundance with the magnetic parameter ranging from $B = 0.01$–1.0 μG. Comparing these results to those from photoionization, the photoionization models still yielded an overall better fit to our observed spectra, as the shock models underpredicted [O II] λ3727 even more than the photoionization models (factor of ∼11 versus a factor of ∼3). Shock models fit [O III] λ4363 marginally better, with a factor of ∼2 too low, versus our CLOUDY models which were a factor of ∼2.6 too low. For [O III] λ5007 our average photoionization models matched within a factor of ∼1 (almost a perfect fit); the shock models matched with an average factor of ∼1.5. Lastly for the [S II] λλ6716, 6731 lines, we modeled with CLOUDY to an average factor of ∼1, while the shock models were off by an average factor of ∼4. Considering the mismatches associated with the shock models, we abandoned the idea of shock ionization being the primary mode of ionization.

We consider the possibility of heating by cosmic rays. Another way to explain the excess [O II] emission is radio plasma within the AGN, which can act as a source of cosmic rays to heat the gas, as previously shown by Ferland & Mushotzky (1984) and Ferland et al. (2009). In order to determine the density of cosmic rays in the handle region, we used our FIRST radio measurements, described in the previous section. The 20 cm flux in the nuclear region corresponds to 20.5 mJy, while the flux in the handle is 5.9 mJy. Since the radio observations were done with a resolution of ∼5″, we are not able to use them to measure the size of the emitting region. Instead, we use the Sloan *i*-band image (Figure 9), assuming that the radio emission

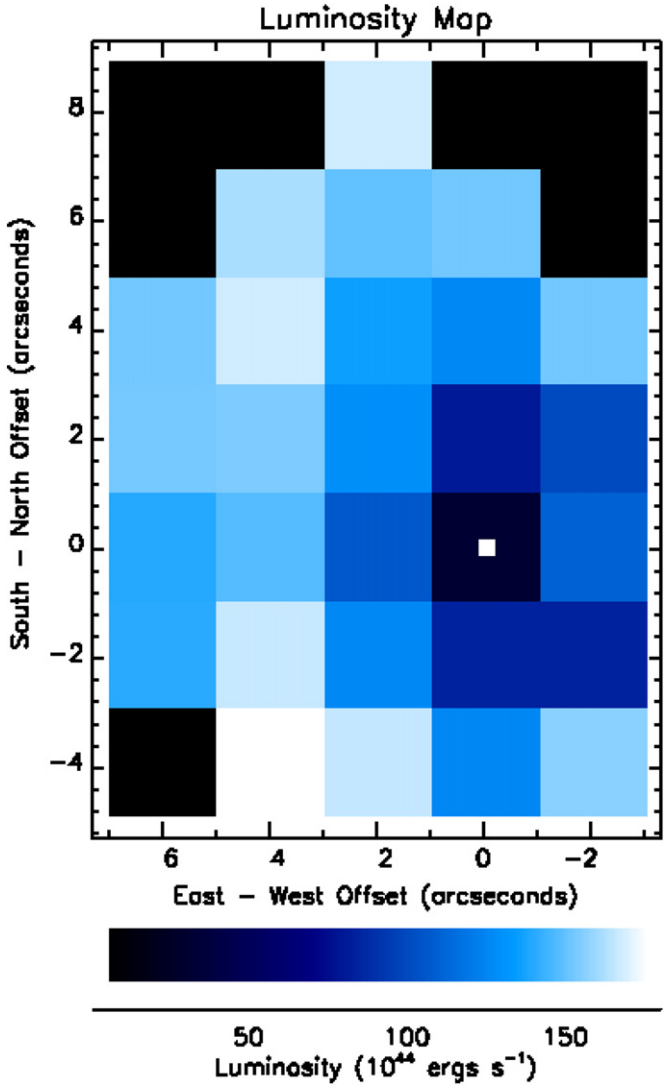

Figure 10. Total luminosity per $2'' \times 2''$ bin calculated from the ionization parameter U and electron density n_H. The small white box gives the location of the nucleus, which has a very low luminosity. The black boxes on the edges contain no data.

(A color version of this figure is available in the online journal.)

is confined inside the handle. We find that the handle has a radius of 1.″7, which corresponds to 2.″83 if one assumes a Gaussian-emitting region. Using the minimum energy equations from Miley (1980), we can calculate the magnetic field inside this region and the pressure and density of relativistic particles (n^*). We assume a spectral index $\alpha = 0.7$, a ratio of energy in heavy particles to the energy in electrons $k = 1$, and a filling factor $\eta = 1$. We find $B_{\rm min} = 1.2 \times 10^{-5}$ G, $P_{\rm rel} = 4.5 \times 10^{-12}$ dyne cm^{-2} and $n_e = 7.1 \times 10^{-9}$ cm^{-3}. These values have a small dependence on the choice of α, k, and η. Using the scale factor $\beta = 10^5$ (Ferland & Mushotzky 1984), which is defined as the ratio of total heating to Coulomb heating, we calculate a density of cosmic rays of $n^* = 10^{-3}$ cm^{-3}. This value can be considered an underestimate, considering the choice of k and η values, so we adopted $\log(n^*) = -2.5$ cm^{-3}.

Returning to our two component CLOUDY models, the expected cosmic ray density of $n^* = 10^{-2.5}$ cm^{-3} was added to the parameters in our low-ionization component. Here we make the assumption that the low-ionization regions of gas have been compressed by radio plasma jets, which results in the low-ionization component having a higher density than the high-ionization component. This assumption also implies that the low- and high-ionization components are displaced from one another with respect to the radio plasma, although they are assumed to be at roughly the same radial distances with respect to the AGNs. The resulting models were able to match the observed strong intensities of [O II] λ3727. However, adding the cosmic rays also added a collisional ionization factor to the gas, boosting the intensities of [N II] λλ6548, 6584 and [S II] λλ6716, 6731 to a factor of 2 or more higher than observed. This unwanted increase in ionization due to collisions can be moderated by applying a scaling law defined by Ferland (1996), which describes how the cosmic ray density at the ionized face of the cloud (n^*) decreases as it propagates through the cloud. This is described by a power law $n^* \propto (r^*)^{\alpha}$, where r^* is the depth of the cloud approximated by $r^* \sim 10 \times (N_H/n_H)$ and we started with power law $\alpha = -2.5$. We then varied values for r^* and α until proper fits were achieved.

5.3. Model Results

Our condition for an acceptable fit between our CLOUDY models and observed spectra was to match the observed lines to within a factor of two or less. This was achieved via two-component CLOUDY models. The observed strong intensity of [O II] λ3727 proved to be a difficult feature to replicate. However, by considering the addition of cosmic rays as a result of radio plasma within the low-ionization gas we were able to increase the levels of [O II] by a factor >3, making it possible to match the observed [O II] intensities as well as the other lines. Modeled values are presented in Tables 3 and 4 in parentheses under observed line intensities. Overall, our modeled line intensities fit our observed data within a factor of two or less. However, the modeled values for [N II] λλ6548, 6583 and [S II] λλ6716, 6731 are often a factor of two or stronger than what is observed. Our modeled values for strong features such as [O III] λ5007 are typically matched to within 90% of the observed intensity or better. Table 5 shows the position for each spectrum, projected distance to the ionizing source ($r_{\rm AGN}$), the high-ionization component values for ionization parameter (U), hydrogen density (n_H), column depth (N_H), cloud depth (r^*), as well as the low ionization parameter values for U, n_H, N_H, r^*, cosmic ray density (n^*), cosmic ray scaling law (α), and r^*. The projected distance ($r_{\rm AGN}$) of the central position is a geometrical approximation as there is no information on where the ionized gas is concentrated within the central resolution element. At (0″, 0″), $r_{\rm AGN} = 1.02$ kpc, which is the average distance from the edge of a 3.4 kpc × 3.4 kpc square to its center.

Errors associated with model input parameters U, N_H, r^*, and n^* were constrained iteratively by incrementally varying their values after achieving a best fit model. Once a model no longer matched our criteria for an acceptable fit, the difference between the incremented parameter values and the best-fit values yielded our errors. Errors for n_H came directly from our errors in measurement for [S II] λλ6716, 6731. The uncertainty in projected distance $r_{\rm AGN}$ is equal to the half width of each bin, as each model's location has been approximated to the central position of each bin.

Once we had acceptable models for each spatially resolved spectrum, we were able to determine $Q(H^0)$ for each $2'' \times 2''$ bin from Equation (6). By integrating our piecewise SED for energies greater than 1 eV, we can derive the ratio of $Q(H^0)$ and bolometric luminosity ($L_{\rm Bol}$). The ratio of $Q(H^0)/L_{\rm Bol} = 6.5 \times 10^9$ photons erg^{-2} allowed us to convert from our calculated $Q(H^0)$ to $L_{\rm Bol}$ seen by the gas at each position.

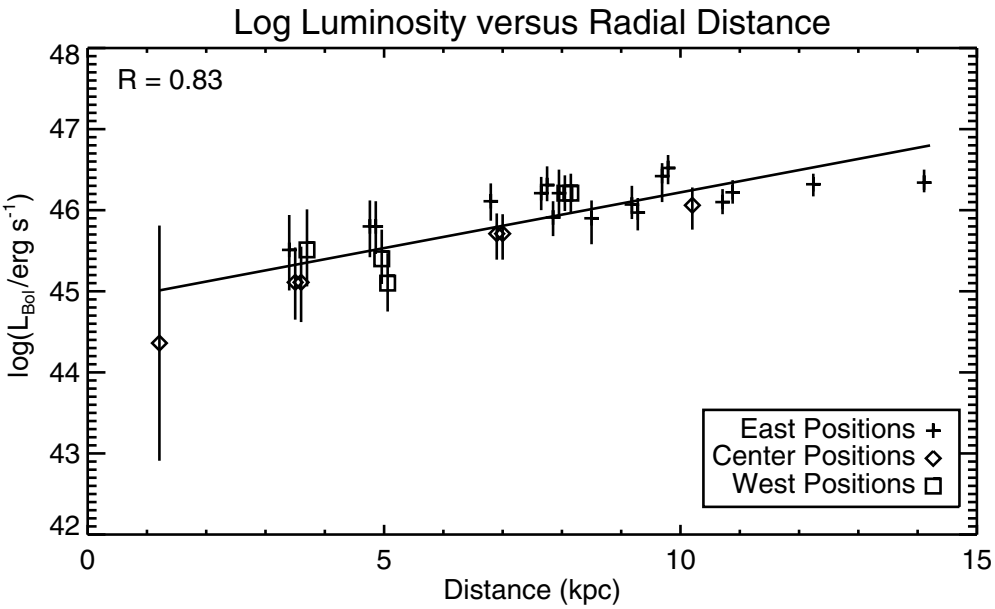

Figure 11. Log of bolometric luminosity for each extracted position broken up by east, west, and center slit positions, plotted vs. relative distance from the nuclear center. Note that for ease of viewing, positions of same relative radius have been slightly offset. A linear fit and correlation coefficient are shown.

Table 5
Projected Distance r_{AGN} as well as U, n_H, and N_H for both Model Components, n^*, α, and r^* for the Low-ionization Component, and L_{Bol}[a]

Position (x'', y'')	r_{AGN} (kpc)	High Ion log(U)	High Ion log(n_H) (cm^{-3})	High Ion log(N_H) (cm^{-2})	Low Ion log(U)	Low Ion log(n_H) (cm^{-3})	Low Ion log(N_H) (cm^{-2})	Low Ion log(n^*) (cm^{-3})	Low Ion α	Low Ion log(r^*) (cm)	log(L_{Bol}) (erg s^{-1})
(5, 4)	10.88	−2.4	$1.8^{+0.50}_{-0.10}$	19.6	−3.4	$2.8^{+0.50}_{-0.10}$	19.7	−2.5	−3.5	18.2	$46.22^{+0.16}_{-0.14}$
(5, 2)	9.18	−2.4	$1.8^{+1.10}_{-0.50}$	19.6	−3.4	$2.8^{+1.10}_{-0.50}$	19.7	−2.5	−3.5	18.2	$46.07^{+0.24}_{-0.18}$
(5, 0)	8.50	−2.3	$1.6^{+0.80}_{-1.70}$	20.5	−3.4	$2.7^{+0.80}_{-1.70}$	19.7	−2.5	−4.0	17.7	$45.90^{+0.22}_{-0.32}$
(5, −2)	9.18	−2.4	$1.7^{+0.50}_{-0.90}$	19.8	−3.5	$2.8^{+0.50}_{-0.90}$	19.7	−2.5	−4.0	17.7	$45.97^{+0.18}_{-0.21}$
(4, 6)	12.24	−2.4	$1.8^{+0.30}_{-0.50}$	19.6	−3.4	$2.8^{+0.30}_{-0.50}$	19.6	−2.5	−3.5	17.7	$46.32^{+0.13}_{-0.15}$
(4, 4)	9.69	−2.4	$2.1^{+0.30}_{-1.80}$	20.4	−3.1	$2.8^{+0.30}_{-1.80}$	20.2	−2.5	−3.5	18.5	$46.42^{+0.16}_{-0.32}$
(4, 2)	7.65	−2.4	$2.1^{+0.30}_{-0.60}$	20.2	−3.2	$2.9^{+0.30}_{-0.60}$	20.1	−2.5	−5.0	18.2	$46.21^{+0.20}_{-0.21}$
(4, 0)	6.80	−2.4	$2.1^{+0.30}_{-0.60}$	20.2	−3.2	$2.9^{+0.30}_{-0.60}$	20.1	−2.5	−5.0	18.2	$46.11^{+0.22}_{-0.24}$
(4, −2)	7.65	−2.3	$2.1^{+0.90}_{-0.30}$	20.5	−3.4	$3.2^{+0.90}_{-0.30}$	19.8	−2.4	−3.5	17.6	$46.31^{+0.23}_{-0.20}$
(4, −4)	9.69	−2.3	$2.1^{+0.50}_{-0.90}$	20.5	−3.4	$3.2^{+0.50}_{-0.90}$	19.8	−2.5	−3.5	17.6	$46.52^{+0.17}_{-0.20}$
(2, 8)	14.11	−2.3	$1.6^{+0.70}_{-0.30}$	20.5	−3.4	$2.7^{+0.70}_{-0.30}$	19.7	−2.5	−4.0	17.7	$46.34^{+0.16}_{-0.12}$
(2, 6)	10.20	−2.3	$1.6^{+0.50}_{-0.30}$	20.5	−3.4	$2.7^{+0.50}_{-0.30}$	19.7	−2.5	−4.0	17.7	$46.10^{+0.16}_{-0.15}$
(2, 4)	7.65	−2.4	$1.8^{+0.40}_{-0.80}$	19.6	−3.4	$2.8^{+0.40}_{-0.80}$	19.7	−2.5	−3.5	18.2	$45.91^{+0.20}_{-0.23}$
(2, 2)	4.76	−2.4	$2.1^{+0.50}_{-1.40}$	20.2	−3.2	$2.9^{+0.50}_{-1.40}$	20.1	−2.5	−5.0	18.2	$45.80^{+0.32}_{-0.38}$
(2, 0)	3.40	−2.4	$2.1^{+0.10}_{-0.70}$	20.2	−3.2	$2.9^{+0.10}_{-0.70}$	20.1	−2.5	−5.0	18.2	$45.51^{+0.44}_{-0.45}$
(2, −2)	4.76	−2.4	$2.1^{+0.20}_{-0.80}$	20.2	−3.2	$2.9^{+0.20}_{-0.80}$	20.1	−2.5	−5.0	18.2	$45.80^{+0.31}_{-0.33}$
(2, −4)	7.65	−2.4	$2.1^{+1.40}_{-1.50}$	20.4	−3.1	$2.8^{+1.40}_{-1.50}$	20.2	−2.5	−3.5	18.5	$46.21^{+0.29}_{-0.30}$
(0, 6)	10.20	−2.3	$1.6^{+1.00}_{-1.60}$	20.5	−3.4	$2.7^{+1.00}_{-1.60}$	19.7	−2.5	−4.0	17.7	$46.06^{+0.22}_{-0.30}$
(0, 4)	6.80	−2.4	$1.7^{+0.80}_{-1.40}$	20.0	−3.4	$2.7^{+0.80}_{-1.40}$	19.7	−2.5	−3.5	18.0	$45.71^{+0.25}_{-0.31}$
(0, 2)	3.40	−2.4	$1.7^{+0.10}_{-0.80}$	19.6	−3.4	$2.7^{+0.10}_{-0.80}$	19.7	−2.5	−3.5	18.0	$45.11^{+0.44}_{-0.45}$
(0, 0)	1.02	−2.4	$1.7^{+0.10}_{-0.70}$	19.6	−3.2	$2.8^{+0.10}_{-0.70}$	20.0	−2.5	−2.5	18.4	$44.36^{+1.45}_{-1.45}$
(0, −2)	3.40	−2.4	$1.7^{+0.50}_{-1.40}$	19.6	−3.4	$2.7^{+0.50}_{-1.40}$	19.8	−2.6	−2.5	18.0	$45.11^{+0.44}_{-0.49}$
(0, −4)	6.80	−2.4	$1.7^{+0.70}_{-1.40}$	19.6	−3.4	$2.7^{+0.70}_{-1.40}$	19.7	−2.5	−3.5	18.0	$45.71^{+0.25}_{-0.31}$
(−2, 4)	7.65	−2.4	$2.1^{+0.40}_{-0.80}$	20.2	−3.2	$2.9^{+0.40}_{-0.80}$	20.1	−2.5	−5.0	18.2	$46.21^{+0.20}_{-0.22}$
(−2, 2)	4.76	−2.4	$2.1^{+0.30}_{-0.10}$	19.6	−3.2	$2.9^{+0.30}_{-0.10}$	20.0	−2.4	−2.0	18.1	$45.40^{+0.31}_{-0.31}$
(−2, 0)	3.40	−2.4	$2.1^{+0.50}_{-0.50}$	20.2	−3.2	$2.9^{+0.50}_{-0.50}$	20.1	−2.5	−5.0	18.2	$45.51^{+0.44}_{-0.44}$
(−2, −2)	4.76	−2.4	$2.1^{+0.50}_{-0.90}$	20.5	−3.2	$2.9^{+0.50}_{-0.90}$	20.1	−2.5	−5.0	18.2	$45.10^{+0.32}_{-0.35}$
(−2, −4)	7.65	−2.4	$2.1^{+0.50}_{-0.90}$	20.2	−3.2	$2.9^{+0.50}_{-0.90}$	20.1	−2.5	−5.0	18.2	$45.21^{+0.21}_{-0.24}$

Note. [a] $\sigma_r = \pm 1.70$ kpc, $\sigma_U = \pm 0.20$, $\sigma_{N_H} = \pm 0.20$ log(cm^{-2}), $\sigma_{n^*} = \pm 0.20$ log(cm^{-3}), $\sigma_\alpha = \pm 0.50$, $\sigma_{r^*} = \pm 0.20$ log(cm).

Table 5 shows the log of the derived bolometric luminosity ($L_{\rm Bol}$) for each modeled position. The errors in $L_{\rm Bol}$ are propagated uncertainties in ionization parameter U, radial distance $r_{\rm AGN}$, and hydrogen density (n_H). For the central region (0″, 0″), $r_{\rm AGN}$ is by far the leading source of error in $L_{\rm Bol}$ due to the large fractional uncertainty in $r_{\rm AGN}$ for this position. The contribution of uncertainty in $L_{\rm Bol}$ decreases quickly for regions at greater distances of $r_{\rm AGN}$.

Figure 10 gives a visual representation of $L_{\rm Bol}$ for each position, which shows that the lowest bolometric luminosities reside at the nuclear center and surrounding regions, while the regions further out and close to the handle seem to be experiencing much higher levels of luminosity. We found the lowest bolometric luminosity at the nuclear center (0″, 0″) to be 2.3×10^{44} erg s^{-1}, more than two orders of magnitude less luminous than that of region (2″, 8″), the furthest region sampled from the source, at which $L_{\rm Bol} = 2.2 \times 10^{46}$ erg s^{-2}, ∼14.1 kpc away from its ionizing source. This drop in luminosity, by a factor greater than 90 over a time frame of $\sim 4 \times 10^4$ yr fits nicely within the time frame of 0.2–2 $\times 10^5$ yr reported by Keel et al. (2012a) for AGNs possessing EELRs such as Hanny's Voorwerp/IC 2497.

Figure 11 plots projected distance from the nucleus in kiloparsecs versus the log of our bolometric luminosities. Note that due to the way our data were sampled, we have multiple extracted bins that share the same radial distance from the nuclear center. Therefore, luminosities at the same radial distance have been offset by ±0.″1 in position to see our error bars. There is no significant differences between east, west, and center points compared to fit. Luminosity increasing with radius as shown in Figures 10 and 11 suggest that the luminosity of the Teacup's central AGN is decreasing dramatically with time.

Although $L_{\rm Bol}$ is a function of U, $r_{\rm AGN}$, and n_H, it is worth pointing out that small deviations of these variables within our observational constraints will still yield the same result of $L_{\rm Bol}$ increasing with radial distance away from the Teacup's nucleus. We find no evidence from our observed spectra that ionization parameter drops off from the central AGN within the observed region. Furthermore, the addition of cosmic rays to our models has no effect on the values used for ionization parameter. Thus, adding cosmic rays does not change the increase in $L_{\rm Bol}$ with radius as calculated from our models.

6. DISCUSSION AND CONCLUSIONS

We have obtained long-slit spectra of the Teacup AGN in the optical range of 3500–9000 Å resulting in spatially resolved spectra. Our kinematic results from the measured [O III] λ5007 centroids suggest primarily galactic rotation, with the major axis of rotation at P.A. ≈ −50°. The area in the NE corner of the galaxy where the EELR is located is redshifted, while the SW area is blueshifted, relative to the galactic nucleus. However the morphology of the galaxy, the dust lane along the rotation axis, and the turnover of the radial velocity curves suggest a more complex situation, possibly due to a merger. Radial velocity plots from KPNO and Lick spectra show a slight bump in velocity over the area of the Teacup's EELR, suggesting there could be something more than galactic rotation acting on the ionized handle. One possibility could be that the EELR is a slow moving outflow. The magnitude of observed velocities is quite low compared to what is normally observed in nearby AGN outflows, (Crenshaw et al. 2000), but this would be an outflow on much larger scales, up to 15 kpc from the nucleus.

From our analysis of BPT diagrams, we were able to diagnose the Teacup as a Type 2 AGN undergoing photoionization. Using CLOUDY, we created photoionization models for a grid of 28 spatially resolved spectra gathered from Lowell observatory. Each spectrum was replicated with composite models consisting of high- and low-ionization components. Our models match our observed emission lines quite well (within a factor of two or less). To achieve acceptable fits to the [O II] emission, we had to include cosmic rays from the radio plasma in our models. The cosmic ray density was approximated using the radio luminosity of this object.

From our CLOUDY models we were able to calculate values of bolometric luminosity for each position, and find that $L_{\rm Bol}$ increases radially from the nuclear center (0″, 0″). We interpret this finding as strong evidence that the central AGN engine decreased in luminosity by a factor ∼90 over a period ∼46,000 yr. Keel et al. (2012a) demonstrated luminosity fading on timescales between 0.2–2 $\times 10^5$ yr for multiple Galaxy Zoo objects with EELRs, including Hanny's Voorwerp and the Teacup AGN. This conclusion was based on the strong ionizing flux needed to create the EELR, the lack of a bright AGNs, and the lack of strong IR flux that would indicate an obscured AGN. Keel et al. concluded that the nuclear IR luminosities are not enough to produce the levels of ionization observed in these object's EELRs, indicating the AGN output has decreased with time. Keel et al. (2012b) then bolstered this claim with a detailed study of the EELR Hanny's Voorwerp and its host galaxy IC2497. Using Space Telescope Imaging Spectrograph (STIS) data, they found that Hanny's Voorwerp exhibits higher levels of ionization in the optical regime than the central AGN of IC2497. Using a combination of X-ray and IR data, Keel et al. are able to derive a spectral energy distribution for the AGN. Once again, they find that the AGN within IC2497 does not possess enough energy to account for observed levels of ionization in Hanny's Voorwerp. Keel et al. (2012b) show that the ionizing luminosity of IC2497's AGN has dropped by a factor of >100 in the last (1–2) $\times 10^5$ yr.

Because we have measured luminosities at multiple distances from the ionizing nucleus, we can extend the analysis to study changes in luminosity over radius and thus time. Our results show a continuous drop in luminosity for the Teacup AGN within a timescale consistent with previous results by Keel et al. Thus, we have additional evidence showing results that agree with previous findings that are independent of IR luminosity arguments.

The Teacup AGN presents two additional interesting characteristics. One is the disturbed morphological loop of the northeast region. The second interesting phenomenon is its extremely strong [O II] λ3727 emission. One possible explanation for both is that the loop was created by expanding radio-jet plasma, consistent with the direction of the current jet, and cosmic rays from the radio plasma also boost the [O II] intensities to what we observe. The galaxy 3C 48 shows both similar morphology and [O II] λ3727/Hβ ratios within its narrow-line region (Stockton et al. 2007). Further studies of these objects might offer new perspectives on the interaction between radio-jet plasma and ionized gas in AGNs.

The EELR around the ionized handle experienced the greatest luminosity, with the location (2″, 8″) being more than 90 times more luminous than the center at ∼46,000 light years away. Considering the change in luminosity across the distance between the nucleus and the NE corner at (2″, 8″), the time frame for the drop in luminosity fits in with previous studies (Keel et al.

2012a, 2012b). From our results, the Teacup's nucleus is dimming at $\sim 4.7 \times 10^{41}$ erg s^{-1} yr^{-1}, so that 46,000 yr ago it was luminous enough to qualify it as a type 2 quasar, while currently the nucleus is in the luminosity regime of a Seyfert 2. From our data presented in Figure 11, we see luminosity is decreasing approximately exponentially. At the current rate at which the Teacup is dimming, it will fall out of the realm of Seyfert luminosity at $\sim 10^{43}$ erg s^{-1}, in another $\sim$470 yr. To further probe the underlying physics behind this change in luminosity, as well the spectacular ionized handle of gas extending out in the north-east corner, further data should be collected. Analysis of high resolution imaging from HST will yield a better look at the extended structure of the handle. X-ray observations would allow a probe of the central AGN, and radio observations would provide the opportunity to look for possible jets, which could be driving the handle.

K.S. gratefully acknowledges support from Swiss National Science Foundation Grant PP00P2_138979/1. J.G. acknowledges K.S. for the naming of the Teacup AGN, and thanks D.M.C. and S.B.K. for their mentorship.

REFERENCES

Allen, M. G., Groves, B. A., Dopita, M. A., Sutherland, R. S., & Kewley, L. J. 2008, ApJS, 178, 20
Asplund, M., Grevesse, N., & Sauval, A. J. 2005, in ASP Conf. Ser. 336, Cosmic Abundances as Records of Stellar Evolution and Nucleosynthesis, ed. T. G. Barnes, III & F. N. Bash (San Francisco, CA: ASP), 25
Baldwin, J. A., Phillips, M. M., & Terlevich, R. 1981, PASP, 93, 5
Becker, R. H., White, R. L., & Helfand, D. J. 1995, ApJ, 450, 559
Best, P. N., Kauffmann, G., Heckman, T. M., & Ivezić, Ž. 2005, MNRAS, 362, 9
Cardelli, J. A., Clayton, G. C., & Mathis, J. S. 1989, ApJ, 345, 245
Crenshaw, D. M., & Peterson, B. M. 1986, PASP, 98, 185
Crenshaw, D. M., Kraemer, S. B., Hutchings, J. B., et al. 2000, AJ, 120, 1731
Crenshaw, D. M., Kraemer, S. B., Bruhweiler, F. C., & Ruiz, J. R. 2001, ApJ, 555, 633
Ferland, G. J., & Netzer, H. 1983, ApJ, 264, 105
Ferland, G. J. 1996, Hazy: A Brief Introduction to Cloudy, Int. Rep. (Lexington: Univ. Kentucky)
Ferland, G. J., Korista, K. T., Verner, D. A., et al. 1998, PASP, 110, 761
Ferland, G. J., & Mushotzky, R. F. 1984, ApJ, 286, 42
Ferland, G. J., Fabian, A. C., Hatch, N. A., et al. 2009, MNRAS, 392, 1475
Fischer, T. C., Crenshaw, D. M., Kraemer, S. B., Schmitt, H. R., & Trippe, M. L. 2010, AJ, 140, 577
Kalfountzou, E., Jarvis, M. J., Bonfield, D. G., & Hardcastle, M. J. 2012, MNRAS, 427, 2401
Keel, W. C., Maksym, W. P., Bennert, V., et al. 2013, NOAO Proposal, 88
Keel, W. C., Chojnowski, S. D., Bennert, V. N., et al. 2012a, MNRAS, 420, 878
Keel, W. C., Lintott, C. J., Schawinski, K., et al. 2012b, AJ, 144, 66
Kewley, L. J., Groves, B., Kauffmann, G., & Heckman, T. 2006, MNRAS, 372, 961
Khachikian, E. E., & Weedman, D. W. 1971, Afz, 7, 389
Kraemer, S. B., Wu, C.-C., Crenshaw, D. M., & Harrington, J. P. 1994, ApJ, 435, 171
Kraemer, S. B., & Crenshaw, D. M. 2000, ApJ, 532, 256
Kraemer, S. B., Crenshaw, D. M., Hutchings, J. B., et al. 2001, ApJ, 551, 671
Miley, G. 1980, ARA&A, 18, 165
Osterbrock, D. E., & Ferland, G. J. (ed.) 2006, Astrophysics of Gaseous Nebulae and Active Galactic Nuclei (2nd ed.; Sausalito, CA: University Science Books)
Stockton, A., Canalizo, G., Fu, H., & Keel, W. 2007, ApJ, 659, 195